

Electron Energy Deposition

1 Transfer equation

The energy - space transfer equation for electrons has the form:

$$\begin{aligned} \mu \frac{\partial I(z, \mu, E)}{\partial z} = & S_{\odot}(z, \mu, E) + n_e(z) \frac{\partial [L(E)I(z, \mu, E)]}{\partial E} + \\ & \int_E^{\infty} \int d\Omega' dE' R(\mu, E; \mu', E') I(z, \mu', E') - \\ & \int_0^E \int d\Omega' dE' R(E, \mu; E', \mu') I(z, \mu, E) \end{aligned} \quad (1)$$

where, μ is the cosine of the pitch angle, I is the intensity in $(cm^{-2}s^{-1}sr^{-1}eV^{-1})$ and z the altitude. The first term on the RHS of the equation is the photoelectron production $(cm^{-3}s^{-1}sr^{-1}eV^{-1})$, the second term describes the degradation of high energy electrons by collisions with thermal electrons, and the last term is the loss of energy E electrons due to all processes leading to lower energy electrons. The third term describes the degradation of high energy electrons through collisions with neutral species that can lead to production of neutrals in excited states, ionization of neutrals and the production of secondary electrons. The processes defining the degradation of energetic electrons and their effect on the energy and pitch angle of the electrons are summarized in Table 1.

If we assume that all locally produced photoelectrons degrade in the same region (no transport effects) the LHS of the equation is zero. Integration over solid angles then gives:

$$\begin{aligned} 0 = & \bar{S}_{\odot}(z, E) + n_e(z) \frac{\partial [L(E)\Phi(z, E)]}{\partial E} + \\ & \int_E^{\infty} \int \int d\Omega d\Omega' dE' R(\mu, E; \mu', E') I(z, \mu', E') \\ & - \int_0^E \int \int d\Omega d\Omega' dE' R(\mu, E; \mu', E') I(z, \mu, E) \end{aligned} \quad (2)$$

where Φ is the omnidirectional flux of electrons $\Phi = \int I d\mu$ $(cm^{-2}s^{-1}eV^{-1})$. If the redistribution function (R) is isotropic the above reduces to the energy dependent only form:

$$\begin{aligned} 0 = & \bar{S}_{\odot}(z, E) + n_e(z) \frac{\partial [L(E)\Phi(z, E)]}{\partial E} + \int_E^{\infty} dE' R(E; E') \Phi(z, E) - \\ & \int_0^E dE' R(E; E') \Phi(z, E) \end{aligned} \quad (3)$$

The last term of all the above equations can be replaced by the total cross

section at energy E , giving eventually:

$$0 = \bar{S}_\odot(z, E) + n_e(z) \frac{\partial[L(E)\Phi(z, E)]}{\partial E} + \int_E^\infty dE' R(E; E')\Phi(z, E) - \sigma_T(E)N\Phi(z, E) \quad (4)$$

where N is the density of the colliding gas. In the above:

$$\bar{S}_\odot = \int S_\odot d\Omega \quad (5)$$

is the production of photoelectrons integrated in all directions.

Tab. 1: Collisional processes affecting the energy and pitch angle of electrons

Collision Type	μ	Energy	New Electron
Elastic			
Scattering by neutrals	Yes	No	No
Inelastic			
Collisions with electrons	No	Yes	No
Excitation of neutrals	Yes	Yes	No
Ionization of neutrals	Yes	Yes	Yes

2 Photoelectron Production

Assuming that the photoionization of neutral species produces photoelectrons symmetrically:

$$S_\odot(z, \mu, E) = \frac{1}{4\pi} S_\odot(z, E) \quad (6)$$

then

$$\bar{S}_\odot = S_\odot(z, E) \quad (7)$$

The photoelectron production at energy E can be calculated from:

$$S_\odot(z, E) = \sum_i F(\lambda) \sigma^{h\nu}(\lambda) q_i^{h\nu}(\lambda) n(z) / \Delta E_\lambda \quad (8)$$

with $F(\lambda)$ the photon flux ($cm^{-2}s^{-1}$), $\sigma^{h\nu}(\lambda)$ the absorption cross section (cm^2) for the photoionized neutral species, $q_i^{h\nu}(\lambda)$ the quantum yield for photoionization process i associated with an ionization potential I_i , $n(z)$ the neutral density and ΔE_λ is the corresponding energy width in eV of the wavelength spectrum. The energy of the produced photoelectron is

$$E = E_\lambda - I_i \quad (eV) \quad (9)$$

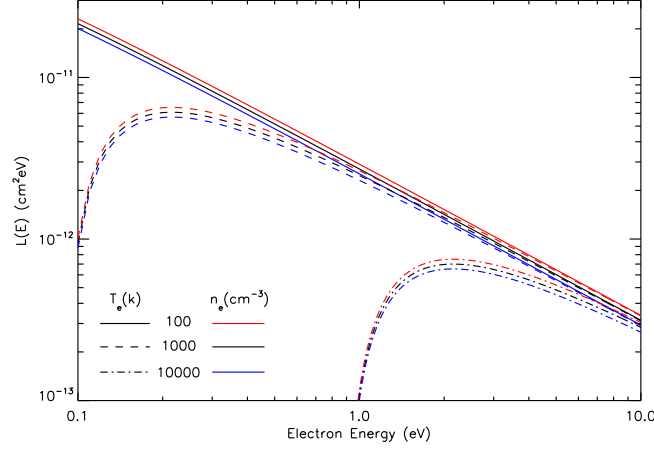


Fig. 1: Variation of electron stopping function with energy for different values of thermal electron temperatures and densities.

3 Collisions with thermal electrons

Electrons with energies larger than 10 eV are degraded mainly through inelastic collisions with the neutral species. For smaller energies the excitation of neutral species has small cross sections and energetic electrons are degraded through collisions with the ambient thermal electrons (mainly Coulomb interactions). The collisions between suprathermal and thermal electrons are described by the stopping function, $L(E)$, (Stamnes and Rees, 1983):

$$L(E) = \frac{3.37 \times 10^{-12}}{E^{0.94} n_e(z)^{0.03}} \left[\frac{E - E_e}{E - 0.53 E_e} \right]^{2.36} \quad (cm^2 eV) \quad (10)$$

with E_e the thermal electron energy which is related with the electron temperature, T_e , through:

$$E_e = k_B T_e = 8.618 \times 10^{-5} T_e \quad (11)$$

4 Inelastic Collisions with neutral species

The redistribution function $R(E, E')$ describes the probability an electron of energy E' going through an interaction with the neutral species to end up with energy E . The possible processes affecting the energy redistribution of the electrons are excitation and ionization with the latter coupled with the production of a secondary electron. For each process the redistribution function takes a different form (Table 2). For an excitation process, the incident electron loses only the energy required to excite a neutral species at a given energy state (W).

Thus, the redistribution function has the form of a delta function that satisfies the energy balance before (E') and after (E) the collision:

$$E' = E + W \quad (12)$$

If the neutral species is ionized by the incident electrons then the remaining energy of the primary electron after the collision depends on the energy of the emerging secondary electron (E_s), described the distribution of secondary electrons (and corresponding emerging degraded primaries) for a specific initial energy E' which again must satisfy the energy balance:

$$E' = E + E_s + I \quad (13)$$

with I the ionization potential of the species for a given state. The energy distribution of the emerging secondary electrons is described by the differential cross section, $\sigma(E_s, E')$ that must satisfy the relationship:

$$\sigma_{Ion}(E') = \int_0^{E'} \sigma(E_s, E') dE_s \quad (14)$$

where σ_{Ion} is the ionization cross section at the energy of the incident electron.

For secondary electron production the differential cross section has been analytically described by fitting experimental results, which for the case of N_2 gave:

$$\sigma(E, E') = \frac{\sigma_{ion}(E')(1 + E/\bar{E})^{-2.1}}{\bar{E} \tanh[(E' - I)/2\bar{E}]} \quad (15)$$

where E and E' are the energies of the secondary and incident electron, respectively, I is the ionization potential and \bar{E} is a spectral shape parameter defined by the measurements ($I=15.6$ eV and $\bar{E}=13.0$ eV for N_2 , $I=12.2$ eV and $\bar{E}=17.4$ eV for O_2). Theoretical calculations have also provided approximate formulas for the secondary electron energy distribution, which for the case of O gave:

$$\sigma(E, E') = \frac{\sigma_{ion}(E')}{WA(E')} \exp \left[-\frac{W}{31.5} - 339 \exp \left(-\frac{W}{2.49} \right) \right] \times \ln \left(\frac{\sqrt{E'} + \sqrt{E' - W}}{\sqrt{E'} - \sqrt{E' - W}} \right) \quad (16)$$

An example of the differential cross section for secondary electron production is given in Fig. 2.

Tab. 2: Redistribution functions for different processes.

Process	R(E,E')
Excitation of neutrals	$\delta(E' - (E + W))\sigma_{exc}(E')n(z)$
Ionization of neutrals	$\sigma_{ion}(E, E')n(z)$
Secondary Electrons	$\sigma_{sec}(E, E')n(z)$

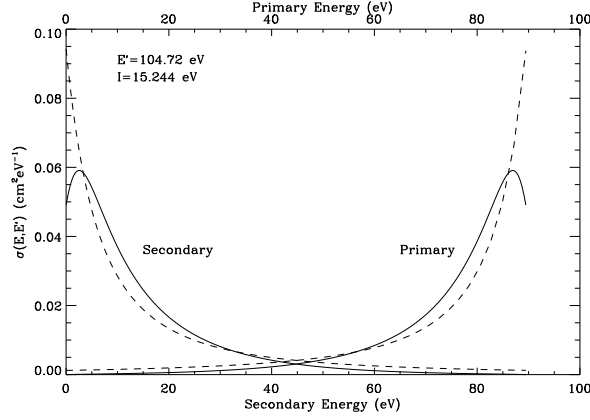


Fig. 2: Differential cross section for secondary electrons using different functions. Dashed lines are calculated through eq. 15 while solid lines are based on eq. 16.

5 Solution Methods

In order to solve for the mean intensity of the electrons with a limited number of energy bins we need to use an expanding grid. In order to discretize equation XX we integrate it over a region of the grid.

5.1 Method 1

Integrating eq. XX over the range of two adjacent energy bins E_j and E_{j+1} and dividing with the total width of the bins, $\Delta E = \Delta E_j + \Delta E_{j+1}$ we get:

$$0 = \frac{1}{\Delta E} \int S(E) dE + \frac{n_e}{\Delta E} \int \frac{\partial [L(E)\Phi(z, E)]}{\partial E} dE + \frac{1}{\Delta E} \int dE \int_E^\infty dE' R(E; E') \Phi(z, E) - \frac{1}{\Delta E} \int dE \sigma_T(E) n(z) \Phi(z, E) \quad (17)$$

Using the values at the mid point of each bin the above results to:

$$0 = \frac{1}{\Delta E} [S(E_j)\Delta E_j + S(E_{j+1})\Delta E_{j+1}] + \frac{n_e}{\Delta E} [L(E_{j+1}^+)\Phi(E_{j+1}) - L(E_j^-)\Phi(E_j)] + \frac{1}{\Delta E} [\Delta E_j f(E_j) + \Delta E_{j+1} f(E_{j+1})] - \frac{n(z)}{\Delta E} [\sigma_T(E_j)\Phi(E_j)\Delta E_j + \sigma_T(E_{j+1})\Phi(E_{j+1})\Delta E_{j+1}] \quad (18)$$

with

$$f(E) = \int_E^{E_{max}} dE' R(E, E') \bar{I}(z, E') \quad (19)$$

Separating the terms for the mean intensity for each bin we get:

$$\alpha_j \Phi(E_j) = \langle S \rangle + \alpha_{j+1} \Phi(E_{j+1}) + \left[\frac{\Delta E_j}{\Delta E} \sum_{m>j} A(j, m) \bar{I}(E_m) + \frac{\Delta E_{j+1}}{\Delta E} \sum_{m>j+1} A(j+1, m) \bar{I}(E_m) \right] \quad (20)$$

with

$$\begin{aligned} \langle S \rangle &= \frac{1}{\Delta E} [S(E_j) \Delta E_j + S(E_{j+1}) \Delta E_{j+1}] \\ \alpha_j &= \frac{n_e}{\Delta E} L(E_j^-) + \frac{\Delta E_j}{\Delta E} n(z) \sigma(E_j) \\ \alpha_{j+1} &= \frac{n_e}{\Delta E} L(E_{j+1}^+) - \frac{\Delta E_{j+1}}{\Delta E} n(z) \sigma(E_{j+1}) \end{aligned} \quad (21)$$

Assuming that $\Phi(E_{max}) = 0$ the above can be solved for all smaller energies.

5.2 Method 2

If we integrate over one bin of our grid centered at energy E and with boundaries (E^+, E^-) we get:

$$0 = S(E) + \frac{n_e}{\Delta E} [L^+ \Phi^+ - L^- \Phi^-] + \frac{1}{2} [f^+ + f^-] - \frac{n(z)}{2} [\sigma_T^+ \Phi^+ + \sigma_T^- \Phi^-] \quad (22)$$

similarly to above but now all terms must be calculated at the boundary energies, except for the photoelectron source term. Thus the above yields the mean intensity at the boundaries of each bin from which the mean intensity at the bin center can be retrieved.

5.3 Energy balance and Grid Corrections

The use of a discrete introduces specific problems in the energy degradation calculations described in detail in Swartz (1985). One way to test the energy conservation through out the grid is by checking that for any bin the energy deposition rate by primary electrons at higher energies equals the rate at which energy is deposited at smaller energies by the degradation of these electrons, plus the rate at which these high energy electrons are losing energy due to excitation of neutral species and collisions with thermal electrons. This, for bin with energy E_i , can be written as:

$$\int_0^{E_i} E P'(E) dE + \int_{E_i}^{\infty} \Phi(E) \sum_{n,j} n_n \sigma_{n,j}(E) W_{n,j} dE + \int_{E_a}^{\infty} \Phi(E) L(E) n_e dE = \int_{E_i}^{\infty} E P_p(E) dE \quad (23)$$

where $P_p(E)$ is the production rate of photoelectrons at energy E and $P'(E)$ is the production rate of electrons (both cascade and secondary) originating from

incident electrons with $E > E_i$. A second criterion has to do with the conservation of the primary electrons: the total production rate of photoelectrons above a specific energy must equal the production rate of cascade electrons at lower energies produced from the degradation of the higher energy electrons. This condition takes the numerical form:

$$\int_{E_i}^{\infty} P_p(E) dE = \int_0^{E_i} P'_c(E) dE \quad (24)$$

where $P'_c(E)$ is the production rate of electrons with energy E due to the ionization or excitation of neutrals by electrons with $E > E_i$.

In order to satisfy these conditions the energy transfer among bins must take into account the width of the bins and the misalignment of the bin centers with the energies of the emerging electrons. In order to solve this problem the real cross sections for each process involved in the calculations must be adjusted with a multiplication factor that will take into account the grid structure. Below are process-specific corrections:

Transition out of bin Suppose that the incident electron has energy E' (which corresponds to the energy of a bin center) and collides with a neutral that is excited to a state with energy W above the ground state. The energy of the emerging electron will then be $E = E' - W$. Yet, within the grid considered this energy falls within the bin centered around E_g . In order to take into account this energy difference, the excitation cross section at energy E' is multiplied by the factor:

$$f_{cor} = \frac{W}{E' - E_g} \quad (25)$$

if $E' - E_g < W$ ($f_{cor} > 1$) then the real emerging electron would have smaller energy than the energy attributed to it by the bin center. Or in term of energy lost, in reality there is large energy lost from the incident electron than the energy loss attributed based on the grid formulation. Thus, in order to adjust for the real energy lost from the initial electron we need to increase the cross section for this process. Similarly, if the transition is an ionization process the cross section must be corrected in the same way but this time the energy of the emerging secondary electron must be taken into account:

$$f_{cor} = \frac{W + E_s}{E' - E_g} \quad (26)$$

Transition within bin If the energy loss for an electron during a collision is smaller than the half width of the bin it belongs then this process will not result in a production of an electron of smaller energy but will be included in the loss of the incident electrons. In order to correct for this problem we need to remove the degraded electron out of the bin artificially. This is done by placing it in the next lower energy bin (at the center of the

bin). In order to conserve energy the cross section for this process must be modified by

$$f_{cor} = \frac{W}{E' - E'_{-1}} \quad (27)$$

This physically means that the grid-adjusted cross section for this process is smaller than the real transition cross section, because we need to have f_{cor} collisions of the incident electron with the neutrals in order to have the energy loss required for the degraded electron energy to fall in the center of the adjacent bin.

Large Bins and big transitions When an electron is degraded by a process that requires energy W , the resulting electron will fall within the bin where the energy $E = E' - W$ falls. E' is the energy at the center of the incident electron bin. If though the incident electron bin is large compared to W , the emerging electron bin will belong to different bins if we consider transitions not from the center but from the edges of the incident electron bin. This means that using the bin center energy for the calculations, in this case results in a deformation of the emerging electron distribution. In order to solve this problem we can sub-divide the incident electron bin into a number of sub-bins and perform the degradation for each bin separately.

The above energy-conservation modifications for the cross sections apply both in the calculation of the emerging electron energies, and the loss rate of electrons. Thus, new cross sections must be calculated for each specific transition and then for the total electron loss at each energy.

6 Transitions and cross sections

The following sections provide a description of the cross sections for photoionization, electron impact and EUV emission for the main molecules, N_2 and CH_4 , present in Titan's atmosphere.

6.1 Photoabsorption

Molecular nitrogen photoabsorption starts close to 1000 Å and absorption down to 800 Å leads to neutral dissociation through the excitation of N_2 to states that strongly pre-dissociate. Lewis et al. (2005) have theoretically investigated the pre-dissociation mechanisms of N_2 and calculated theoretical cross sections for the neutral photodissociation. The high resolution cross sections suggest that the absorption is dominated by transitions between specific states that results to multiple narrow band systems with the lack of a continuum absorption. These values need to be averaged over a high resolution photon flux spectrum in order to have a correct calculation of the N_2 photolysis rate (Fig. 3). The products of the photodissociation depend on the states involved in the predissociation process and a complete understanding of these mechanisms is not yet achieved. Theoretical calculations suggest that the ultimate predissociation channel is the

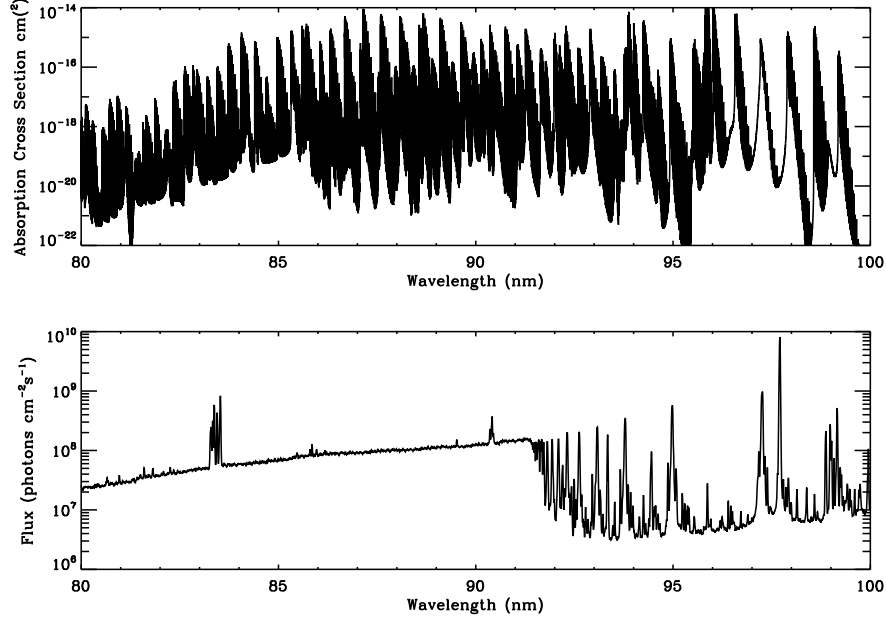


Fig. 3: Theoretically calculated cross sections of N_2 photoabsorption between 80 and 100 nm from Lewis et al. (2005) (upper panel) and high resolution solar flux spectrum from the SOHO/SUMER instrument (lower panel).

$C' \ ^3\Pi_u$ state that leads to $N(^2D) + N(^4S)$ formation (Lewis et al., 2005). Thus, we assume in the calculations that neutral dissociation provides only these two products in equal amounts.

The threshold for N_2^+ formation is at 796.8 \AA (15.58 eV), and at this energy N_2^+ is produced in its ground state ($X \ ^2\Sigma_g^+$). Higher photon energies lead to the production of the N_2 ion at excited states. The analysis of the emerging photoelectron spectra show specific band formation that is correlated with the excitation of the ions to specific states depending on the energy of the photons (see Table 3). For wavelengths smaller than 510 \AA (24.3 eV) the excited N_2^+ ions have enough energy to dissociate initiating the dissociative photoionization. The ionization of the valence electrons leading to the X, A and B bands leads to the formation of N_2^+ , while the ionization of the inner-valence electron leads to production of the C, F, E, G and H bands which are related to the dissociative photoionization. The total ionization and dissociative ionization cross sections have been measured by Samson et al. (1987) (Fig. 4), while the cross sections for the excitation of the N_2^+ ions at the different bands originating from the inner-valence electrons have been reported by Krummacher et al. (1980) for the C, F, E and the combined G+H bands. In the calculations we have normalized the cross sections of Krummacher et al. (1980) to the total dissociative ionization

Tab. 3: Band nomenclature of the N₂ ionization emerging photoelectrons and the threshold energy. Data from Baltzer et al. (1992) and Krummacher et al. (1980).

Band	Threshold energy (eV)	Products
X $^2\Sigma_g^+$	15.58	N ₂ ⁺
A $^2\Pi_u$	16.926	N ₂ ⁺
B $^2\Sigma_u^+$	18.751	N ₂ ⁺
C $^2\Sigma_u^+$	25.514	see text
F $^2\Sigma_g^+$	28.8	N ⁺ (³ P) + N(² D)
E $^2\Sigma_g^+$	33.6	N ⁺ (³ P) + N(² D)
G+H	36.8	N ⁺ (³ P) + N(² D)

cross sections reported by Samson et al. (1987). The state of the dissociation fragments produced depends also on the photon energy. This has been investigated by Nicolas (2003) for the C band and by Aoto et al. (2006) for higher bands. For the C band, from the dissociation limit up to 473 Å (26.19 eV) the products are N⁺(³P) + N(⁴S), while at smaller wavelengths until 464.6 Å (26.68 eV) the yield for the last channel drops to 40% and the rest 60% is in the N⁺(¹D) + N(⁴S) channel. The authors also report a narrow region between 26.275 and 26.3 eV where the two channels have equal yields. At even lower energies the dissociation products are in the N⁺(³P) + N(²D) states. For the other bands the measurements of Aoto et al. (2006) suggest that the emerging dissociation products can be at different states as the ionization energy increases. In the calculations we consider production only in the N⁺(³P) + N(²D) states.

The cross sections for the photolysis of methane are taken from different laboratory investigations depending on the wavelength region investigated. Photoionization and dissociative photoionization cross sections were measured from (Samson et al., 1989) between 110 and 950 Å and provide yields for all the main dissociation products. The main ion fragments produced at all wavelengths are CH₄⁺ and CH₃⁺ (Fig. 5). CH₂⁺ production starts at 816.0 Å (15.2 eV) accompanied with a hydrogen molecule. Below 630.3 Å (19.67 eV) the hydrogen molecule can be further dissociated to atomic hydrogens, but whether this happens or not could not be retrieved from the observations. In the calculations we assumed that below 630.3 Å we have 50% yield for each of the two processes. For all the other dissociation ion products we assume the neutral products to be those at the first threshold energy, although further dissociation can produce different neutral fragments at higher energies (see Table 5 taken from Samson et al. (1989)). The absorption cross section for wavelengths below the C K-edge (43.68 Å) can be described by the functional:

$$\ln \sigma(Mb) = 2.494 \times \ln[\lambda(\text{\AA})] - 9.307, \quad (28)$$

while the cross sections at lower energies are taken from other laboratory measurements described in Samson et al. (1989). The yields for the different channels below 110 Å are assumed to remain constant to the measured values at

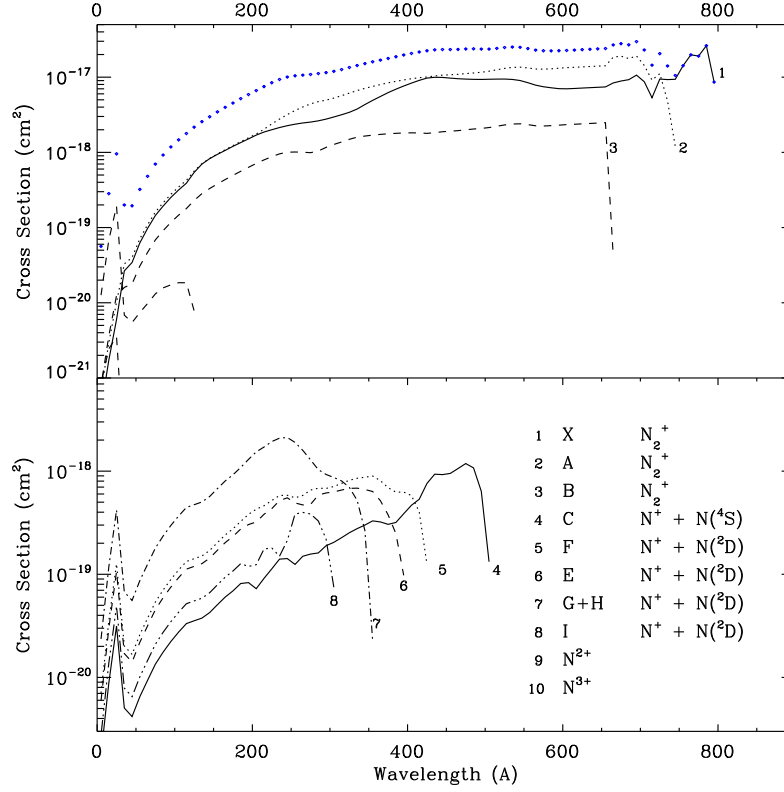


Fig. 4: N_2 cross sections for ionization and dissociative ionization (see text for references) .

110 Å. At lower energies, neutral photodissociation is assumed to provide fragments based on the laboratory measurements of Wang et al. (2000) at Ly- α (Table 4). The total photoabsorption cross sections above the ionization threshold are taken from Lee and Chiang (1983) and Mount et al. (1977).

Tab. 4: Methane photolysis products at Ly- α

Products	Yield
$CH_3 + H$	0.291
$^1CH_2 + H_2$	0.584
$^1CH_2 + 2 H$	0.055
$CH + H_2 + H$	0.07

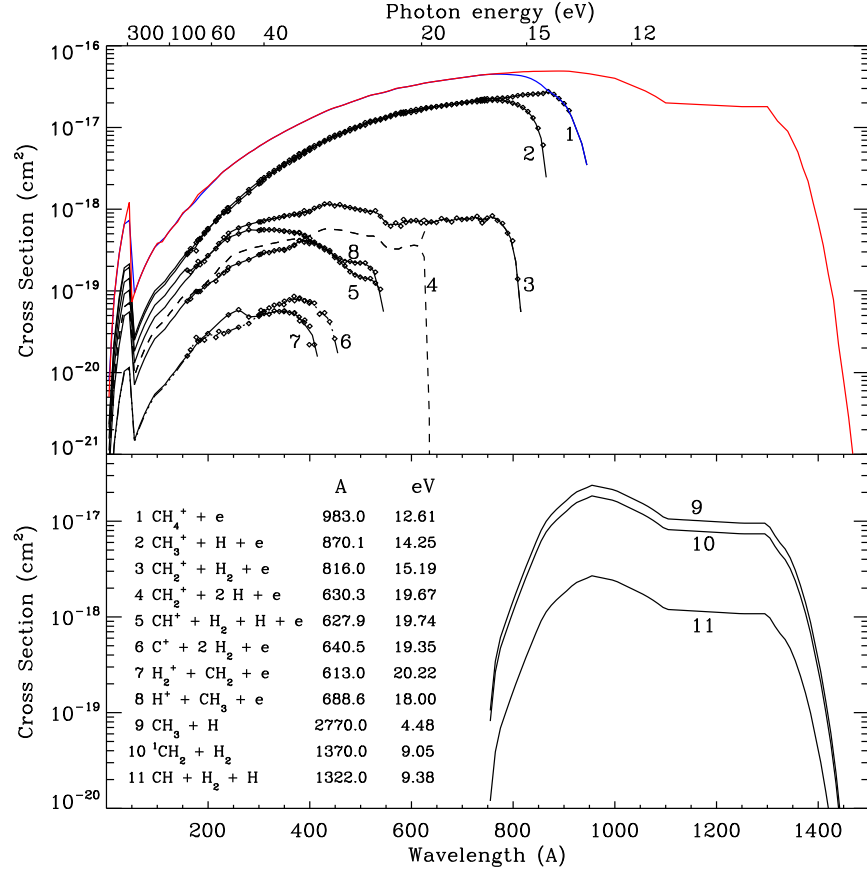


Fig. 5: CH_4 photolysis cross sections. The red and blue lines correspond to the total absorption and total ionization cross sections, while the numbers present different ionization products summarized in the captions along with the thresholds for each channel.

Tab. 5: Energy thresholds for different products of methane dissociative photoionization (Samson et al., 1989).

Products		eV	Å
CH_4^+		12.61	983.0
CH_3^+	+ H	14.25	870.1
CH_2^+	+ H_2	15.20	816.0
	+ 2 H	19.67	630.3
CH^+	+ H_2 + H	19.75	627.9
	+ 3 H	24.22	511.9
C^+	+ 2 H_2	19.36	640.5
	+ H_2 + 2 H	23.83	520.2
	+ 4 H	28.31	437.9
H_2^+	+ CH_2	20.23	613.0
	+ C + H_2	23.52	527.1
	+ CH + H	24.53	505.4
	+ C + 2 H	28.00	442.8
H^+	+ CH_3	18.01	688.6
	+ CH + H_2	22.70	546.1
	+ CH_2 + H	22.80	542.0
	+ C + H_2 + H	26.17	473.7
	+ CH + 2 H	27.18	456.1
	+ C + 4 H	30.65	404.5

6.2 Electron Impact

The electron impact cross sections for nitrogen and methane are presented in Figures 6 & 7. The measurements for the cross sections of N_2 are taken from the latest review of Itikawa (2006), which includes all the processes excited by electron impact (rotational, vibrational, electronic excitations, and ionization). The state specific ionization cross sections for N_2 are taken from Shemansky and Liu (2005). The cross sections for methane are based on the electron impact ionization cross sections of Liu and Shemansky (2006) and the scaling law from the theoretical work of Erwin and Kunc (2005, 2008). The latter provides estimates for the electron impact dissociation cross sections of methane based on the measured cross sections for ionization. The cross sections for the vibrational excitation of methane are taken from Davies et al. (1989). The products of dissociation are summarized in Table 6.

6.3 EUV and FUV emission

The interaction of photons and electrons with molecules leaves the latter in an excited state and/or dissociates them producing fragments in excited states as well. Under low pressure conditions collisional de-excitation is not efficient and the de-excitation proceeds through the emission of photons (fluorescence) the wavelength of which depends on the states involved. For Titan's atmosphere

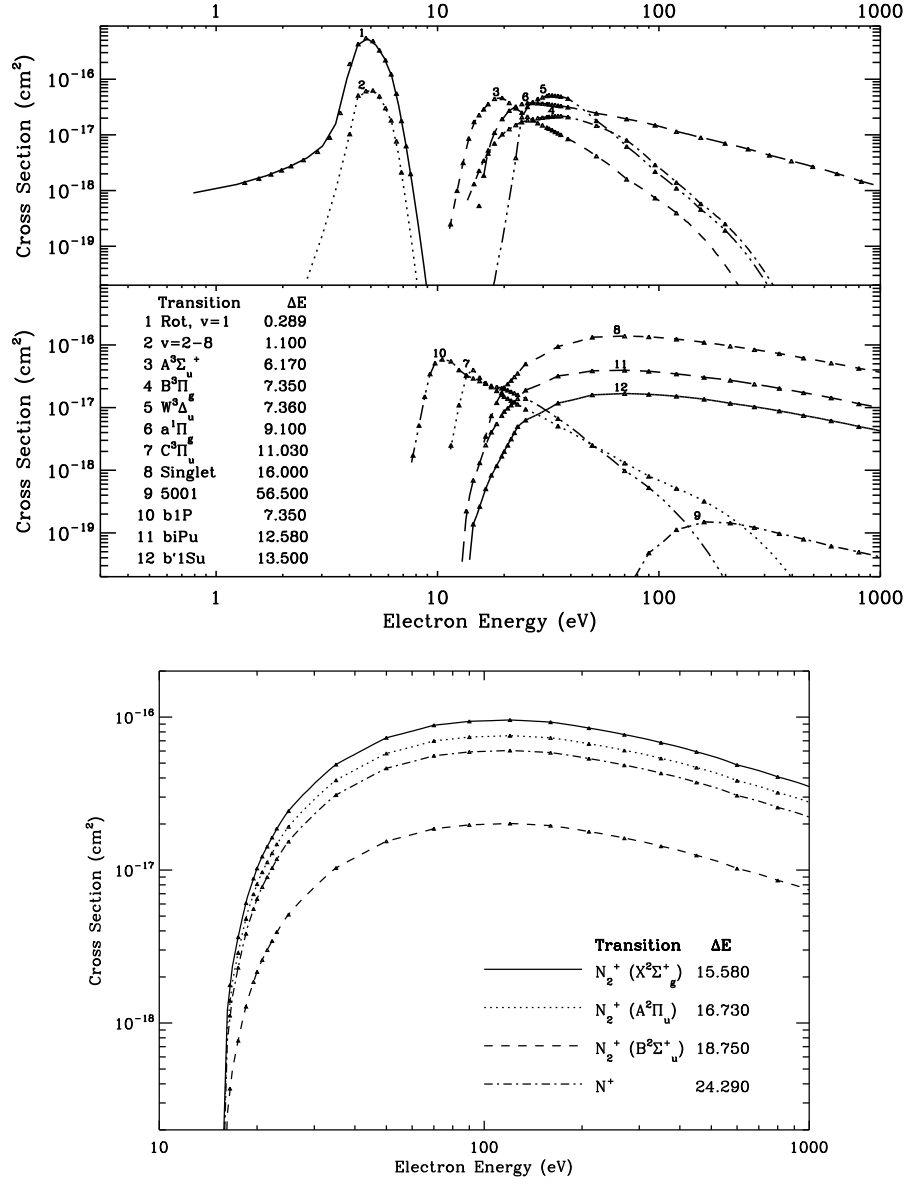
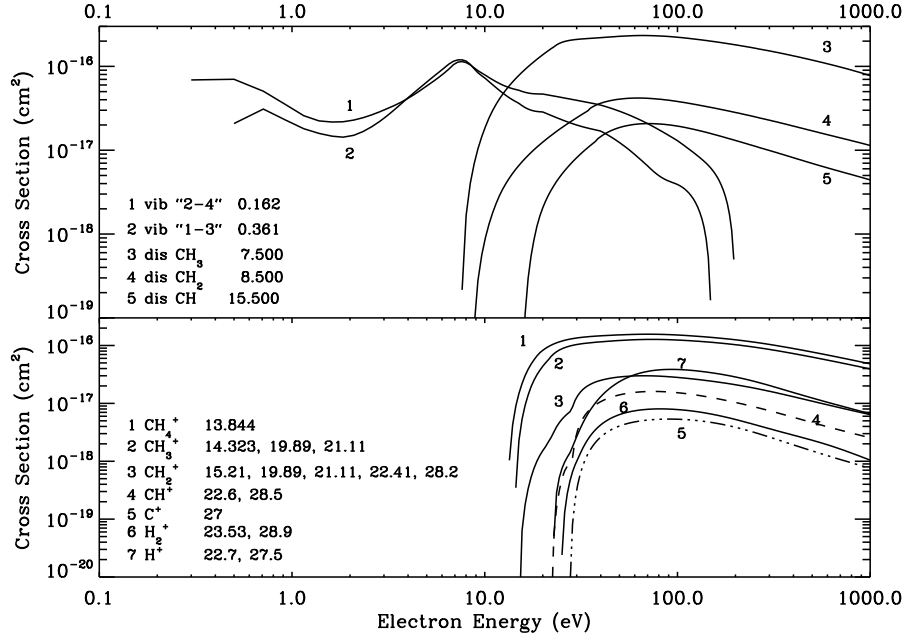


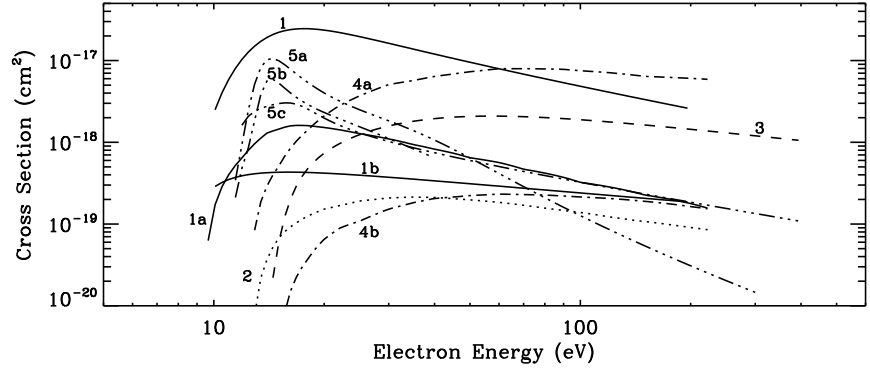
Fig. 6: N_2 electron impact cross sections for excitation (upper panel) and ionization (lower panel). The possible transitions along with the threshold energy for each state are given.

Tab. 6: Products and threshold energies for electron impact on N₂ and CH₄.

N ₂ state	Threshold	Products	CH ₄ state	Threshold	Product
N ₂ Rot j=0→2	1.48×10^{-3}	N ₂ [*]	Vib 2-4	0.162	CH ₄ [*]
N ₂ Vib v=0→1	0.289	N ₂ [*]	Vib 1-3	0.361	CH ₄ [*]
N ₂ A ³ Σ _u ⁺	6.169	N ₂ [*]	Dis	7.5	CH ₃ + H
N ₂ B ³ Π _g	7.353	N ₂ [*]	Dis	8.5	¹ CH ₂ + 2 H
N ₂ W ³ Δ _u	7.362	N ₂ [*]	Dis	15.5	CH + H ₂ + H
N ₂ B' ³ Σ _u ⁻	8.165	N ₂ [*]	Ion	13.844	CH ₄ ⁺ + e
N ₂ α' ¹ Σ _u ⁻	8.399	N ₂ [*]	Ion	14.323	CH ₃ ⁺ + H + e
N ₂ α ¹ Π _g	8.549	N ₂ [*]	Ion	19.890	CH ₃ ⁺ + H + 2e
N ₂ w' ¹ Δ _u	8.890	N ₂ [*]	Ion	21.11	CH ₃ ⁺ + H + 2e
N ₂ C ³ Π _u	11.032	N(² D) + N(⁴ S)	Ion	15.21	CH ₂ ⁺ + 2H + 2e
N ₂ E ³ Σ _g ⁺	11.875	N(² D) + N(⁴ S)	Ion	19.89	CH ₂ ⁺ + 2H + 2e
N ₂ α'' ¹ Σ _g ⁺	12.255	N(² D) + N(⁴ S)	Ion	21.11	CH ₂ ⁺ + 2H + 2e
N ₂ b' ¹ Π _u	12.500	N(² D) + N(⁴ S)	Ion	22.41	CH ₂ ⁺ + 2H + 2e
N ₂ b' ¹ Σ _u	12.854	N(² D) + N(⁴ S)	Ion	28.20	CH ₂ ⁺ + 2H + 2e
N ₂ c ₄ ' ¹ Σ _u ⁺	12.935	N(² D) + N(⁴ S)	Ion	22.60	CH ⁺ + H ₂ + H + 2e
N ₂ ⁺ X ² Σ _g ⁺	15.581	N ⁺ + N(⁴ S)	Ion	28.50	CH ⁺ + H ₂ + H + 2e
N ₂ ⁺ A ² Π _g	16.699	N ⁺ + N(⁴ S)	Ion	27.00	CH ⁺ + H ₂ + H + 2e
N ₂ ⁺ B ² Σ _u ⁺	18.751	N ⁺ + N(⁴ S)	Ion	23.53	H ₂ ⁺ + CH ₂ + 2e
			Ion	28.90	H ₂ ⁺ + CH ₂ + 2e
			Ion	23.70	H ⁺ + CH ₃ + 2e
			Ion	27.50	H ⁺ + CH ₃ + 2e

Fig. 7: CH₄ electron impact cross sections

the EUV and FUV emissions observed are dominated by N₂ features. Samson et al. (1991) and Meier et al. (1991) used synchrotron radiation to measure the N₂ fluorescence at multiple wavelengths. They found that the observed emitted radiation originated from the de-excitation of excited N and N⁺ fragments produced by the dissociative photoionization of N₂. All of the emission lines were correlated with N₂ excitation in the H band (see photoabsorption cross sections) which totally dissociates. Thus, it was possible to derive relative yields and emission cross sections for each line emission based on measured cross section for this band. This analysis assumes that there is no wavelength structure of the emission cross section relative to the H-band cross section. Also, emission at the observed wavelengths can also originate from neutral dissociation (N(⁴S)+N*) or from higher excited states (N⁺* + N* or N⁺* + N⁺) but these processes have very low efficiency and probability, respectively. Emissions at wavelengths beyond the detection limit of Meier et al. (1991) were also attributed to the same process. A complete list is given in Table 7 with values taken from Bishop and Feldman (2003). Photoelectron impact on N₂ provides also significant UV emissions, some of them not allowed by photons such as the Lyman-Birge-Hopfield band. Reviews of emission cross sections for different transitions are reported in the literature (Itikawa, 2006; Tabata et al., 2006). A compilation of the cross sections used is presented in Fig. 8.



Band Name	Transition	$\lambda(\text{\AA})$	key
Lyman-Birge-Hopfield	$\alpha \text{ } ^1\Pi_g \rightarrow \text{X } ^1\Sigma_g^+$	Total	1
		(3,3)	1a
		(3,0)	1b
		(1,2)	2
Birge-Hopfield I	$b \text{ } ^1\Pi_u \rightarrow \text{X } ^1\Sigma_g^+$	Total	3
Birge-Hopfield II	$b' \text{ } ^1\Sigma_u^+ \rightarrow \text{X } ^1\Sigma_g^+$	857-945	4a
Carroll-Yoshino	$c_s \text{ } ^1\Sigma_u^+ \rightarrow \text{X } ^1\Sigma_g^+$	958	4b
		(16,0)	5a
2 nd Positive	$C \text{ } ^1\Pi_g \rightarrow A \text{ } ^1\Sigma_g^+$	(0,0)	5b
		(1,0)	5c
		(0,2)	

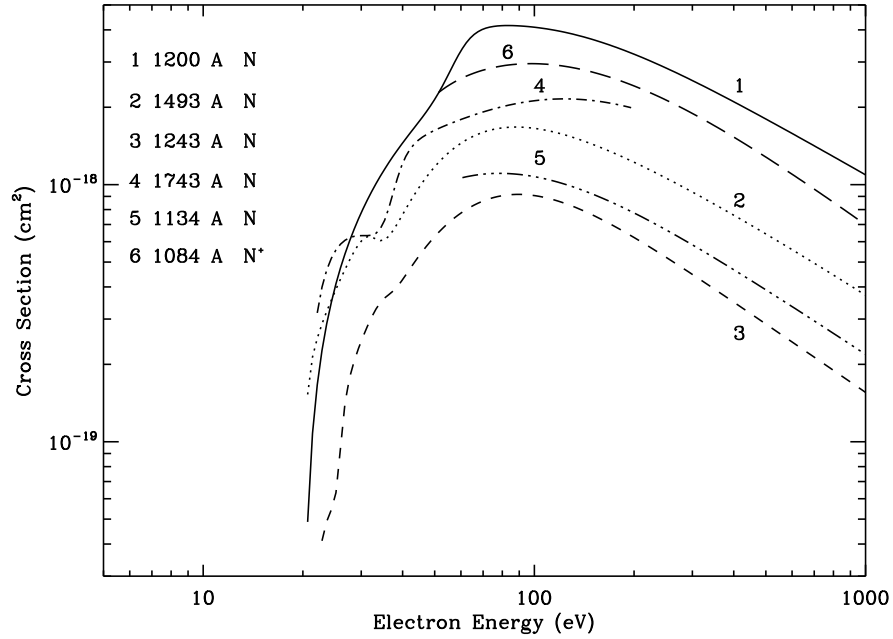


Fig. 8: Emission cross sections for photoelectron impact on N_2 . Upper panel is for de-excitation of N_2^+ states and lower panel for de-excitation of N and N^+ states.

Tab. 7: Emission lines and relative intensities observed from the photodissociative ionization of N_2 in the H band. The values are taken from Bishop and Feldman (2003) where the neutral and ion atomic states involved can also be found. Boldface numbers correspond to wavelengths in Å and roman to relative intensities measured.

N								N ⁺	
1743	0.043	1319	0.012	1177	0.008	1096 - 1098	0.009	2143	0.063
1493	0.110	1310	0.015	1168	0.015	1067 - 1069	0.007	2139	0.037
1412	0.008	1243	0.035	1134	0.045	1051 - 1053	0.003	1085	0.110
1327	0.004	1200	0.310	1100	0.005	1043 - 1044	0.003	916	0.036

7 Comparison between Local Approximation and Transfer calculations

The local approximation used in the current formulation has its limitations. At high neutral densities the collisions between energetic electrons and gas species are rapid enough to spatially constrain their energy deposition in the local region defined by the photoelectron production. As the atmospheric density decreases towards higher altitudes, the collisions between the energetic electrons and the neutral species become (relatively) less frequent and the former can diffuse in the atmosphere for large distances between collisions. This effect is evident in the comparison between the electron fluxes calculated with the two methods at different altitudes (Fig. 9a). At low altitudes the agreement between the two methods is very good, but above 1200 km differences start to appear. The same is evident in the altitude profile of the electron production rate (Fig. 9b).

8 Validation against Cassini measurements

The Cassini spacecraft provided for the first time high resolution *in situ* measurements for the electron fluxes and EUV/FUV emissions in Titan's atmosphere which can be used for validation of our simulations.

8.1 CAPS Electron flux measurements

The CAPS/ELS instruments measured the electrons fluxes along different altitudes during each Titan flyby (?). We validate our electron fluxes model against the T40 flyby measurements. We use the neutral densities of N_2 and CH_4 measured by INMS for this flyby and scale them upward by a constant factor of 2.6 which is found necessary on order to have the INMS measured densities in agreement with the atmospheric density derived by the HASI and the Cassini Attitude and Articulation Control Subsystem (AACCS) observations. During the flyby CAPS also detected the presence of negative ions, every time the actuator of the instrument was pointing in the ram direction of the spacecraft (Fig. 10). Thus, we can compare the instrument measurements with the simulation results

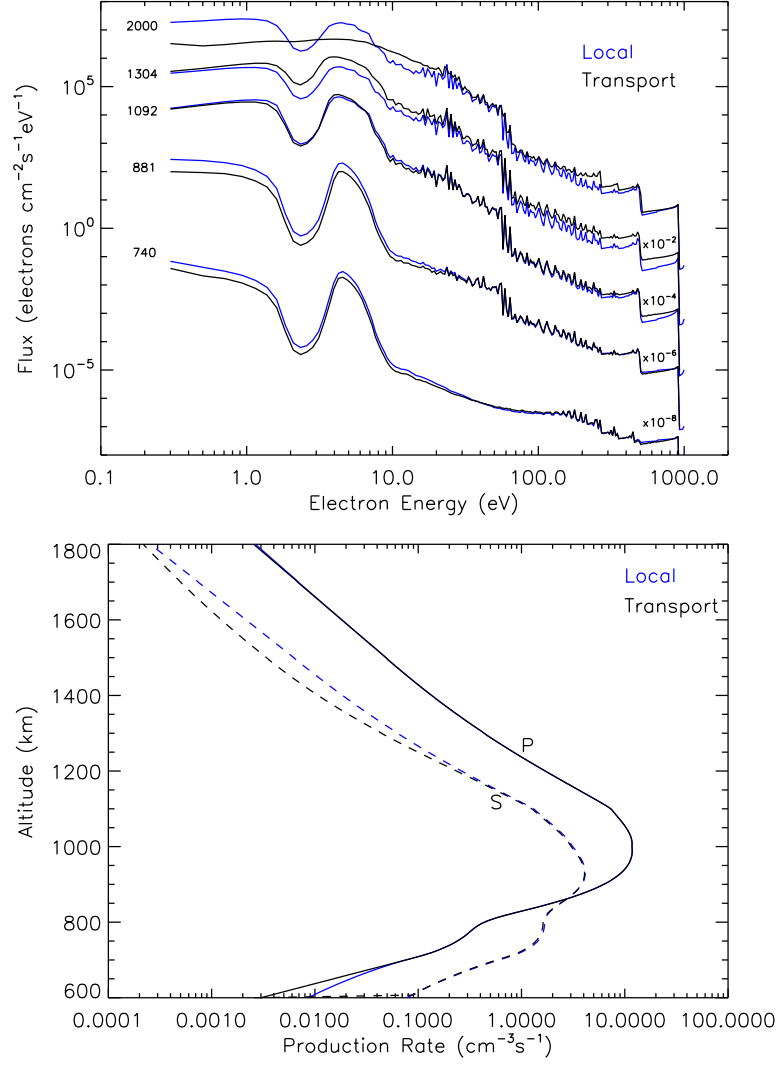


Fig. 9: Upper panel: Comparison between local approximation model and transport calculations at different altitudes. Lower paner: Primary and secondary electron production rates for the local approximation and transport calculations.

only at altitudes not affected by the negative ions (see Fig. 11). The largest number of spectra available for the averaging are found around the closest approach. The comparison between the model and observations can be separated into three energy regions: $E < 5$ eV, $5 \text{ eV} < E < 15$ eV, and $E > 15$ eV. The best agreement between the model and the observations takes place in the second energy region ($5 \text{ eV} < E < 15$ eV) where both the magnitude and energy dependence of the differential electron flux are well reproduced. The local peak close to 24 eV is due to strong He II (304 Å) solar line which provides a strong photoelectron production at this energy range. This feature is composed of three peaks originating from the ionization of N_2 in the three valence states (X, A, and B), but these can not be resolved by the energy resolution of the CAPS instrument ($\Delta E/E = 16.7\%$). For larger energies there is a sharp decrease in the electron flux based on the model calculations although the observations suggest a significantly large flux of electrons that is decreasing rather slowly with increasing energy. It is interesting to note that structure of the high energy fluxes is very similar to the energy variation of the one count level which for the number of spectra added for the closest approach averaging is very close to the observed differential flux. Thus, this part of the observations appear to be an instrument artifact. A contribution of magnetospheric electrons could also affect the measurements in this energy range. CHECK ENERGY OF MAGNETOSPHERIC ELECTRONS AND DISCUSS POSSIBLE EFFECTS. For the smaller energy range measured by CAPS ($E < 5$ eV) the most prominent feature observed is the maximum between 4 and 5 eV related with the vibrational excitation of N_2 . The location of the nearby minimum based on the model results should be at 2.3 eV but the observations suggest a minimum at a slightly smaller energy. In addition the magnitude of the flux is different between the model and the observations between the peak and the trough. The first discrepancy is related with the value of the spacecraft potential used in the retrieval of the electron fluxes. The results presented here assume a -0.5 eV for the spacecraft potential but close inspection of the location of the HeII photoelectron peak suggest a large value which would bring the location of the minimum in the low energy in good agreement with the observations. In addition, plasma instabilities related to the sharp decrease of the photoelectron density in this region are known to affect the resulting energy distribution. This has been observed in Earth's atmosphere as well, but no rigorous correction method has been used so far. Thus, in the energy range where the observations are reliable, the model appears to be in good agreement with them while, the discrepancies observed are related with well-known issues.

++ SOLAR FLUX, SOLAR ZENITH ANGLE VARIATION

8.2 UVIS EUV and FUV emission measurements

The Cassini UltraViolet Imaging Spectrometer (UVIS) provided measurements of the EUV and FUV emissions from Titan's disk (Ajello et al., 2007, 2008). The published emissions are from the second Titan flyby (TB) on December 13th, 2004. We compare the observed emissions with our model results for a

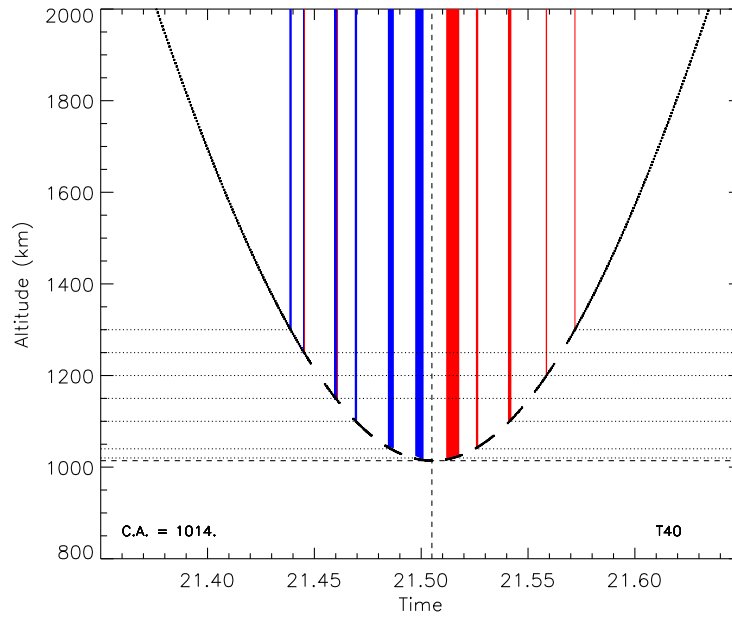


Fig. 10: Cassini spacecraft trajectory during T40 flyby (black line). The gaps correspond to the times where the actuator was in the ram direction and negative ions are detected. The red and blue shaded regions correspond to the altitudes where we compare the measurements with the model results for the ingress (blue) and egress (red) parts of the flyby. The dashed line marks the altitude of closest approach.

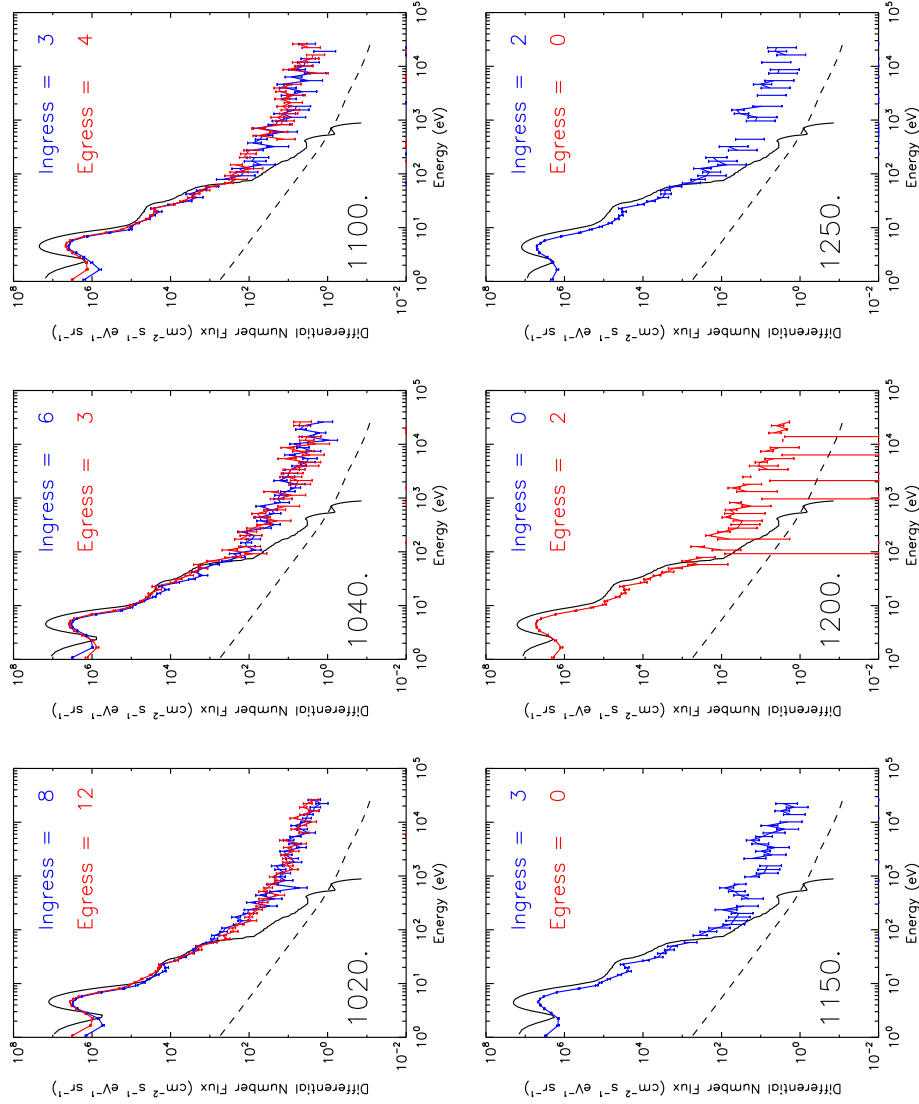


Fig. 11: Comparison between measured and calculated with local-approximation model electron fluxes in Titan's atmosphere during the T40 flyby. The solid black line correspond to the model results for the altitude shown in each panel. The unidirectional fluxes calculated by the local model are divided by 4π in order to compare with the measured differential fluxes. The red and blue lines correspond to the average measured fluxes for the ingress and egress parts of the flyby. The averaging is performed by the combination of all available measured spectra ± 5 km from the reference altitude. The available number of spectra is given in each panel. the error bars correspond to the uncertainty of the averaged spectra assuming Poisson statistics. The dashed line corresponds to the one count level in units of differential flux. This has to be multiplied by the time span of each observation (~ 2 sec) and the number of spectra used for the averaging.

solar zenith angle of 60° , which is closest to the disk average observations. For the case of photoelectron impact, the volume emission rate for each line, at each altitude, $P_\lambda(z)$, is calculated from:

$$P_\lambda(z) = \int \Phi(E) \sigma_\lambda(E) n(z) dE \quad (29)$$

with $\Phi(E)$ the electron flux at energy E , σ_λ the emission cross section at wavelength λ for electron impact, and $n(z)$ the N_2 number density at altitude z . A similar expression is used for the volume emission rates by photon induced transitions. Some of the lines observed by UVIS are generated by both photon absorption and electron impact, while others are specific to the processes generating them (LBH band). Fig. 12 presents the volume emission rates from different excited states of N_2^+ excited by photoelectron impact. The dominant emission from the optical forbidden Lyman-Birge-Hopfield (LBH) band ($\alpha^1\Pi_g \rightarrow X^1\Sigma_g^+$) is located in the FUV region, while the other bands are observed in the EUV region. The altitude dependence of the rates reflects the electron production rates described above, with a peak above 1000 km from primary photoelectrons and a shoulder close to 800 km due to secondary electron production. The corresponding volume emission rates from the excited dissociation fragments of N_2 (N^* and N^{+*}) are presented in Fig. 13 for both photon and photoelectron induced transitions, with the former having a significantly larger contribution than the latter.

The emission observed by UVIS corresponds to the integrated volume emission along the line of site. They correspond to measurements of Titan's disk, thus we calculated the model intensity for nadir viewing, taking into account the attenuation of the emitted photons from N_2 and CH_4 absorption. The resulting FUV intensities are presented in Table 8 and compared with the observations. Considering that the calculated emissions are an upper limit, due to the specific nadir viewing relative to the disk average UVIS observations, there is a very good agreement between observations and experiment. We note also that for increasing wavelengths of emitted radiation, the agreement becomes better because the attenuation due to atmospheric absorption becomes smaller. The emissions at the EUV regions from the excited N_2^+ states are subject to multiple scattering of the Carroll-Yoshinko band ($c'_4{}^1\Sigma_u^+ \rightarrow X^1\Sigma_g^+$) and requires more complicated calculations (Stevens, 2001; Ajello et al., 2007). These are beyond the scope of the current work where we only attempt to validate our model calculations. Thus, the validation of the model calculations against both the UVIS and CAPS observations confirms the well reproduction of the energetic processes in Titan's upper atmosphere by our calculations.

9 Production Rates

As discussed above the interaction of photons and photoelectrons with the gas-phase molecules leads to the production of a large number of radicals in the atmosphere. Further chemical reaction of these radicals provides the multitude

Tab. 8:

Band/Line (\AA)	MODEL			UVIS
	Photons	Photoelectrons	Total	
1085	1.92	0.35	2.27	2.31
1135	0.88	0.09	0.96	1.33
1200	6.62	1.03	7.65	6.8
1243	0.75	0.26	1.01	0.6
1493	2.35	0.73	3.08	3.0
1743	0.90	0.87	1.77	1.6
Total NI	14.70	3.64	18.34	16
LBH (1250-2600)	-	41.24	41.24	43 ± 7

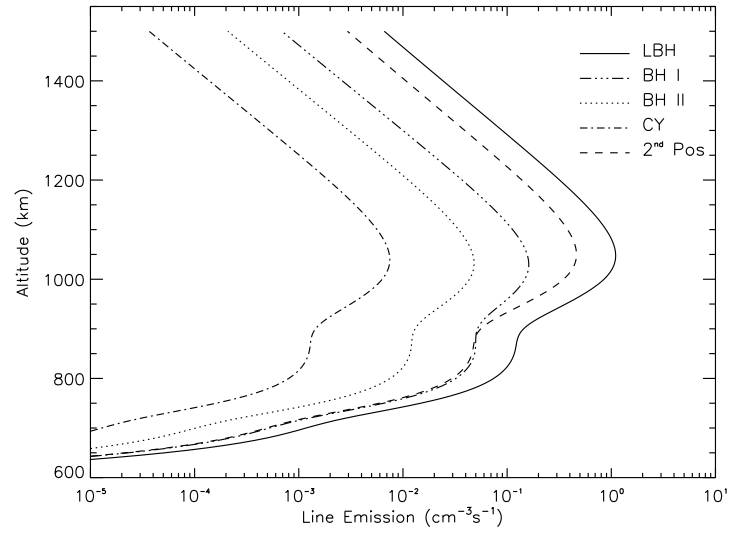
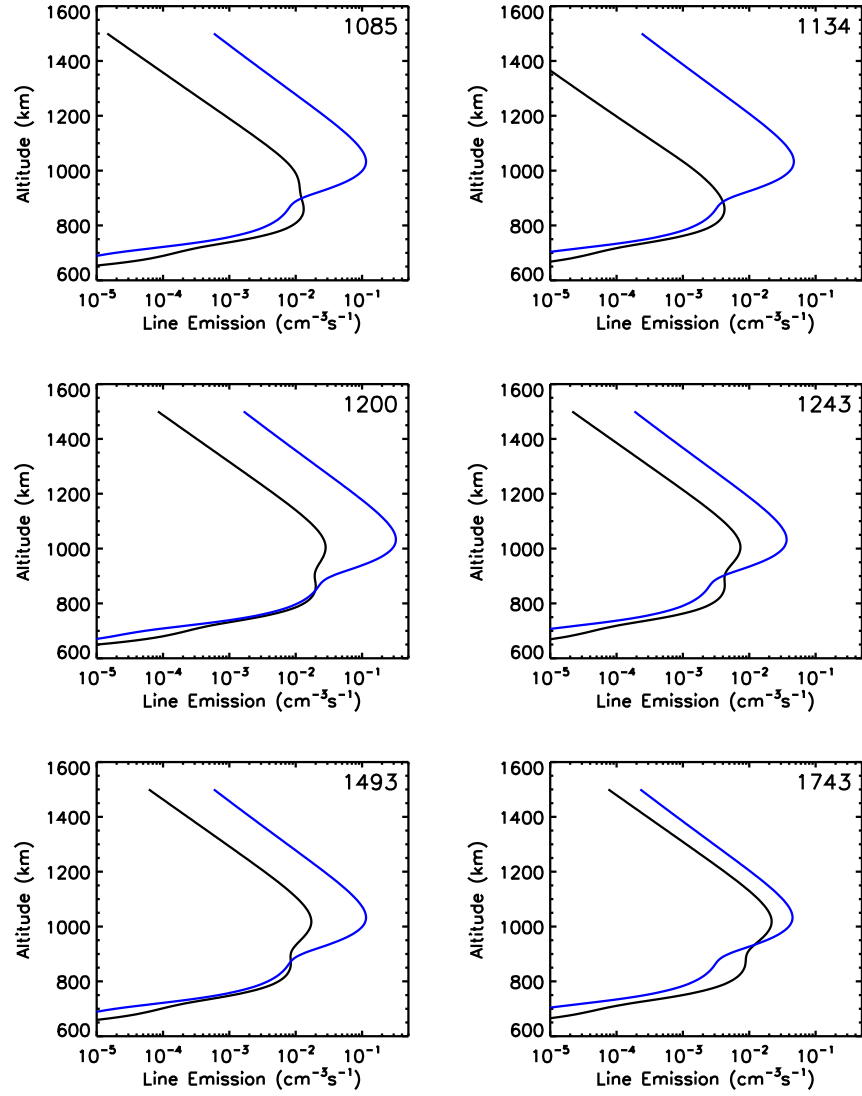


Fig. 12: Volume emission at different bands of N2 due to photoelectrons impact.

Fig. 13: Volume emission by atomic N and N^+ .

Tab. 9: Column production rates for each fragment of the dissociation of N_2 and CH_4 .

Product	Photolysis	Photoelectrons	Total
N_2^+			
N^+			
$\text{N}(^4\text{S})$			
$\text{N}(^2\text{D})$			
CH_4^+			
CH_3^+			
CH_2^+			
CH^+			
C^+			
CH_3			
$^1\text{CH}_2$			
CH			

of chemical species observed in Titan's atmosphere. Thus, identifying the produced radicals and the rate at which they are generated in the atmosphere is imperative in order to have a correct description of the subsequent chemistry. For disk average calculations ($\text{SZA} = 60^\circ$) the resulting production rates of radicals from N_2 and CH_4 are presented in Fig. 14. For N_2 photons have a peak contribution at ~ 1000 km, while the contribution of photoelectrons becomes dominant between 700 and 900 km due to the production of secondary electrons. Thus, both dissociation sources are required for the description of the total N_2 loss rate. For methane, due to the larger extend of its absorption spectrum to longer wavelengths compared to N_2 we get different picture. Ionization by photons peaks at 1000 km, as for N_2 , but neutral dissociation by photons extends to lower altitudes with a maximum at ~ 800 km. Photoelectrons, produced in the region of ionization, dissociate methane at 1000 km (primary photoelectrons) and at 700 - 900 km (secondary photoelectrons) providing a dominant ion production in the latter region but do not significantly affect the total production of neutral fragments.

The column production rates for each radical/ion produced are presented in Table 9.

References

- Ajello, J.M., and 9 co-authors, 2007. Titan airglow spectra from Cassini Ultraviolet Imaging Spectrograph (UVIS): EUV analysis. *Geophys. Res. Lett.*, 34, L24202, doi: 10.1029/2007GL031555.
- Ajello, J.M., and 9 co-authors, 2008. Titan airglow spectra from Cassini Ultraviolet Imaging Spectrograph: FUV analysis. *Geophys. Res. Lett.*, 35, L06102, doi: 10.1029/2007GL032315.

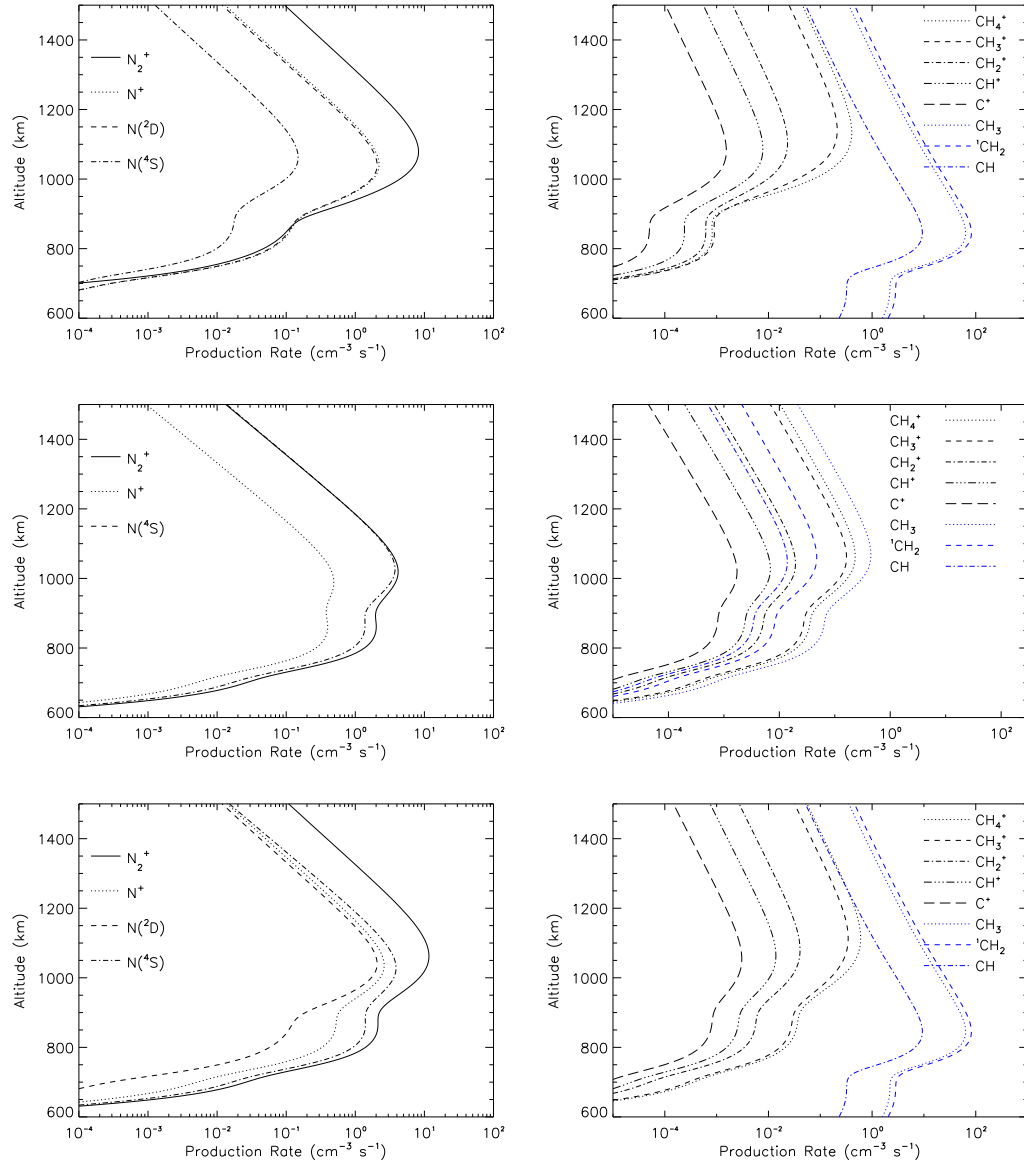


Fig. 14: Productions rates of different dissociation products of N_2 and CH_4 due to photons (top row), photoelectrons (middle row) and cumulative (bottom row).

- Aoto, T., Ito, K., Hikosaka, Y., Shibasaki, A., Hirayama, R., Yamamono, N., Miyoshi, E., 2006. Inner-valence states of N_2^+ and the dissociation dynamics studied by threshold photoelectron spectroscopy and configuration interaction calculation. *J. Chem. Phys.*, 124, 234306.
- Baltzer, P., Larsson, M., Karlsson, L., Wannberg, B., Carlsson Gothe, M., 1992. Inner-valence states of N_2^+ studied by uv photoelectron spectroscopy and configuration-interaction calculations. *Phys. Rev. A*, 46, 5545-5553.
- Bishop, J., Feldman, P.D., 2003. Analysis of the Astro-1/Hopkins Ultraviolet Telescope EUV-FUV dayside nadir spectral radiance measurements. *J. Geophys. Res.*, 108, 1243, doi: 10.1029/2001JA000330.
- Davies, D.K., Kline, L.E., Bies, W.E., 1989. Measurements of swarm parameters and derived electron collision cross sections in methane. *J. Appl. Phys.*, 65, 3311-3323.
- Erwin, D.A., and Kunc, J.A., 2005. Electron-impact dissociation of the methane molecule into neutral fragments. *Phys. Rev. A*, 72, 052719.
- Erwin, D.A., and Kunc, J.A., 2008. Dissociation and ionization of the methane molecule by nonrelativistic electrons including the near threshold region. *J. Applied Phys.*, 103, 064906.
- Itikawa, Y., 2006. Cross sections for electron collisions with nitrogen molecules. *J. Phys. Chem. Ref. Data*, 35, 31-53.
- Krummacher, S., Schmidt, V., Wulleumier, F., 1980. Inner-shell photoionization in molecules: the nitrogen case. *J. Phys. B*, 13, 3993-4005.
- Lee, L.C., Chiang, C.C., 1983. Fluorescence yield from photodissociation of CH_4 at 1060-1420 Å. *J. Chem. Phys.*, 78, 688-691.
- Lewis, B.R., Gibson, S.T., Zhang, W., Lefebvre-Brion, H., Robbe, J.-M., 2005. Predissociation mechanism for the lowest $^1\Pi_u$ states of N_2 . *J. Chem. Phys.*, 122, 144302.
- Liu, X., and Shemansky, D.E., 2006. Analysis of electron impact ionization properties of methane. *J. Geophys. Res.*, 111, A04303.
- Meier, R.R., Samson, J.A., Chung, Y., Lee, E.-M., He, Z.-X., 1991. Production of N^{+*} from $N_2 + h\nu$: Effective EUV emission yields from laboratory and dayglow data. *Planet. Space Sci.*, 39, 1197-1207.
- Mount, G.H., Warden, E.S., Moos, H.W., 1977. Photoabsorption cross sections of methane from 1400 to 1850 Å. *Ap. J.*, 214, L47-L49.
- Nicolas, C., Alcaraz, C., Thissen, R., Vervloet, M., Dutuit, O., 2003. Dissociative photoionization of N_2 in the 24-32 eV photon energy range. *J. Phys. B*, 36, 2239-2251.

- Rees, H.M. 1989. Physics and chemistry of the upper atmosphere. Cambridge university press.
- Samson, J.A.R., Masuoka, T., Pareek, P.N., Angel, G.C., 1987. Total and dissociative photoionization cross sections of N_2 from threshold to 107 eV. J. Chem. Phys., 86, 6128-6132.
- Samson, J.A.R., Haddad, G.N., Masuoka, T., Pareek, P.N., Kilcoyne, D.A.L., 1989. Ionization yields, total absorption, and dissociative photoionization cross sections of CH_4 from 110-950 Å. J. Chem. Phys., 90, 6925-6932.
- Samson, J.A., Chung, Y., Lee, E.-M., 1991. Excited ionic and neutral fragments produced by dissociation of $N_2^+ H$ band. J. Chem. Phys., 95, 717-719.
- Shemansky, D.E., Liu, X., 2005. Evaluation of electron impact excitation of $N_2 X^1\Sigma_g^+(0)$ into the $N_2^+ X^2\Sigma_g^+(\nu)$, $A^2\Pi_u^+(\nu)$, and $B^2\Sigma_u^+(\nu)$ states. J. Geophys. Res., 110, A07307, doi:10.1029/2005JA011062.
- Stamnes, K., Rees, M.H., 1983. Heating of thermal ionospheric electrons by suprathermal electrons. Geophys. Res. Let., 10, 309-312.
- Stevens, M.H., 2001. The EUV airglow of Titan: Production and loss of $N_2 c_4(0)-X$. J. Geophys. Res., 106, 3685-3689.
- Swartz, W.E. 1985. Optimization of energetic electron energy degradation calculations. JGR, 90, 6587-6593.
- Tabata, T., Shirai, T., Sataka, M., Kubo, H., 2006. Analytic cross sections for electron impact collisions with nitrogen molecules. Atomic Data Nucl. Data Tabl., 92, 375-406.
- Wang, J.-H., Liu, K., Min, Z., Su, H., Bersohn, R., Preses, J., Larese, J.Z., 2000. Vacuum ultraviolet photochemistry of CH_4 and isotopomers. II. Product channel fields and absorption spectra. J. Chem. Phys., 113, 4146-4152.